BJRS
BRAZILIAN JOURNAL OF RADIATION SCIENCES

doi.org/10.15392/2319-0612.2025.2573
2025, 13(1) | 01-31 | e2573
Submitted: 2024-07-23
Accepted: 2025-15-01

A Monte Carlo Simulation study on the design and optimization of collimators for non-collinear cascade gamma-ray correlation emissions in medical imaging

Nkuba [a*], L. L.; Lugendo [b], I. J.

[a] Nuclear Technology and Technical Services Directorate, Tanzania Atomic Energy Commission, P.O. Box 1585, Block AF, Plot No. 634, Atomu Road, Mnadani Street, Kikombo Area, 41206, Dodoma, Tanzania.
[b] Department of Physics, University of Dar es Salaam, Physics Building, Uvumbuzi Road, P.O. Box 35063, Dar es Salaam, Tanzania.

*Correspondence: leonid_nkuba@yahoo.co.uk

Abstract: This study focused on designing and optimizing collimators for cascade gamma-ray imaging through Monte Carlo simulations. The trapezoidal-shaped collimator blocks, designed in the Geant4 application for emission tomography (GATE) environment, were attached to a simulated small animal GATE - PET model. The collimators were optimized by simulating septa thicknesses from 0.2 mm to 1.2 mm, in 0.2 mm increments. A 1.0 MBq ^{111}In source having radius of 0.25 mm was used as the cascade gamma-ray emitter. Sixteen trapezoidal tungsten collimator blocks were designed, each with a 16.31 mm × 37.5 mm surface facing the detector crystals, and a 12.33 mm × 37.5 mm surface facing the scanned object. Each block featured 105 parallel rectangular holes arranged in a 7 × 15 array, with a length of 10.0 mm, resulting in a ring-like collimator with a 41.0 mm outer radius. The designed collimator, intended for small animal imaging, prioritizes resolution. Hence, a collimator with 1.0 mm septa and hole sizes of 1.5 mm × 0.7 mm, offering spatial resolutions of 7.6 mm and 4.1 mm in the axial and transaxial directions, respectively, was chosen. The collimators demonstrated energy resolution of approximately 8.96% and 10.10% at 171.3 keV and 245.4 keV, respectively, within a 10% energy resolution threshold set during simulations. Besides, the reconstructed source positions ranged from 81.1% to 100% of the true simulated source positions within the field of view. The optimized collimator design presents a viable solution for imaging small animals' internal organs, with sizes exceeding 7.6 mm.

Keywords: GATE Monte Carlo simulation, Cascade gamma-rays, Optimized collimator design, and Medical image reconstruction.

BJRS
BRAZILIAN JOURNAL OF RADIATION SCIENCES

doi.org/10.15392/2319-0612.2025.2573
2025, 13(1) | 01-31 | e2573
Submitted: 2024-07-23
Accepted: 2025-15-01

Estudo de simulação Monte Carlo sobre o projeto e otimização de colimadores para emissões de correlação de raios gama em cascata não colineares em imagens médicas

Resumo: Este estudo focou-se no desenho e otimização de colimadores para imagem com raios gama em cascata através de simulações de Monte Carlo. Os blocos de colimadores em forma trapezoidal, foram projetados na aplicação Geant4 GATE, para um ambiente de tomografia por emissão de pôsitrons (PET). Os colimadores foram acoplados a um modelo simulado de PET para pequenos animais, e foram otimizados simulando espessuras de septos de 0,2 mm a 1,2 mm, em incrementos de 0,2 mm. Uma fonte de ^{111}In com raio de 0,25 mm e atividade de 1,0 MBq foi usada como emissor de raios gama em cascata. No GATE, dezesseis blocos de colimadores de tungstênio trapezoidais foram desenhados, cada um com uma superfície de 16,31 mm × 37,5 mm de face para os cristais do detector, e uma superfície de 12,33 mm × 37,5 mm de face para o objeto escaneado. Cada bloco contém 105 orifícios retangulares paralelos dispostos em uma matriz de 7 × 15, com comprimento de 10,0 mm, resultando em um colimador em forma de anel com um raio externo de 41,0 mm. O colimador assim desenhado, destinado à imagem de pequenos animais, prioriza a resolução. Assim, um colimador com septos de 1,0 mm e tamanhos de orifício de 1,5 mm × 0,7 mm, com resoluções espaciais de 7,6 mm e 4,1 mm nas direções axial e transaxial, respectivamente, foi escolhido. Além disso, os colimadores demonstraram boa resolução de energia de ~8,96% e ~10,10% para 171,3 keV e 245,4 keV, respectivamente, dentro de um limite de resolução de energia de 10% estabelecido durante as simulações. Também, dentro do campo de visão, as posições reconstruídas da fonte variaram de 81,1% a 100% das posições reais simuladas. O desenho otimizado do colimador apresenta uma solução viável para imagem dos órgãos internos de pequenos animais, com tamanhos superiores a 7,6 mm.

Palavras-chave: Simulação de Monte Carlo, GATE, Raios gama em cascata, Desenho otimizado de colimadores e Reconstrução de imagens médicas.

1. INTRODUCTION

The decay of some radionuclides employed in nuclear medicine often involves the simultaneous emission of two or more gamma-rays [1] and, occasionally, a gamma-ray along with a *K* x-ray [2]. Typically, these gamma rays are referred to as being emitted in a cascade. The time interval between the emission of the first and second gamma-ray is marked by an intermediate state with a half-life of up to tens of nanoseconds [3, 4]. For instance, the $7/2 \rightarrow 5/2 \rightarrow 1/2$ cascade in the decay of ^{111}In to ^{111}Cd, after ^{111}In undergoes electron cupture has the intermediate state with half life of 85 ns while the $3/2^{+} \rightarrow 5/2^{-} \rightarrow 7/2^{-}$ decay cascade of ^{43}Ca (in exicited state) after ^{43}K undergoes beta minus decay, has an intermediate state with half-life of 48 ps [1, 2, 5, 6]. These cascade gamma-rays are emitted successively and share a common emission point. Consequently, detecting the cascade gamma-rays in coincidence offers potential for medical imaging, as they can be used to create images using the gamma-gamma coincidence imaging technique [1, 2, 7]. The use of cascade gamma-rays allows the determination of a three-dimensional (3D) decay vertex of a single decay event, a capability that is lacking in single photon emission computed tomography (SPECT) and positron emission tomography (PET) imaging systems [6-9].

Unlike positron emitters, which produce collinear annihilation photons, gamma rays from decay cascades often exhibit significant non-collinearity [1, 8, 10]. Hence, cascade gamma-rays typically lack strong angular correlation [2]. As a result, coincidence detection often requires collimated detectors in certain cases [11]. However, a major limitation of coincidence imaging with cascade gamma-rays is the reduced geometric efficiency [12]. To overcome this limitation, an imaging system consisting of *n* collimated detectors surrounding the source has been proposed [12]. In order to maximize the system's geometric efficiency, the designed collimators were integrated into a small animal PET scanner of Rikagaku Kenkyūsho (RIKEN) as described by Yamamoto et al. [13].

In small animal imaging systems like the one we have developed, spatial resolution is a crucial parameter, particularly due to the small size of the organs being imaged [14]. For example, clinical gamma cameras (SPECT and scintigraphy imaging) can achieve a spatial resolution of about one centimeter under working conditions using parallel hole collimation [15]. Therefore, for collimated small animal imaging, a spatial resolution of a few millimeters or sub-millimeters is necessary. For this reason, multi-pinhole collimators are prefered over parallel-hole collimators because they are capable of offering higher spatial resolution ranging in a few submillimeters and greater sensitivity compared to parallel-hole collimators [16].

Despite their higher spatial resolution and greater sensitivity, multi-pinhole collimators exhibit varying spatial resolution across the field of view (FoV) because they collect data from different angles [16]. Yet, parallel-hole collimators have a large FoV, and their sensitivity does not decrease with distance, making them very suitable for whole-body scanning [16]. Therefore, since in this work we aimed for consistent spatial resolution across the FoV with the use of a simple image reconstruction algorithm [1, 17, 18], parallel-hole collimators were studied. In particular, the current study aimed at designing and optimizing parallel hole collimators for cascade gamma-ray imaging. The design and optimization of the collimators were conducted using Monte Carlo simulations. While numerous simulation codes are available for simulating collimator parameters, detection systems, and other aspects of imaging systems in nuclear medicine [19], the GATE codes are considered more suitable for this purpose due to their designed capacity to simulate various imaging parameters, including detector collimators [20].

2. MATERIALS AND METHODS

2.1. Small animal PET and its GATE simulation model

The small animal PET scanner, whose geometric characteristics and detector material composition are given in Table 1, has been extensively described [13, 21, 22, 23]. The aforementioned small animal PET assembly is mainly used for research purposes.

Table 1: The geometric characteristic of a RIKEN Small animal PET assembly

ITEMS	DESCRIPTION
Detector material	GSO (Ce)
Dimensions of the Lower/First layer of crystals (mm^3)	1.6 × 2.4 × 7
Dimensions of the Upper/Second layer of crystals (mm^3)	1.6 × 2.4 × 8
Crystal Array	11 × 15
Crystal pitch (mm)	1.7 × 2.5
Number of crystals per detector (module)	165
Number of detectors (modules) in the system	16
The outer diameter of the prototype (mm)	130
The inner diameter of the prototype (mm)	95
Axial field of view (mm)	37.5

In the GATE simulation, after defining the scanner and its components, as shown in Figure 1, the definition of the collimators and phantoms followed, as well as the physical processes occurring in the collimator, crystals and phantoms.

Figure 1: The simulated GSO detector of a small animal PET scanner. The detector pixel (crystal) matrix and crystal layers (module) are shown [23].

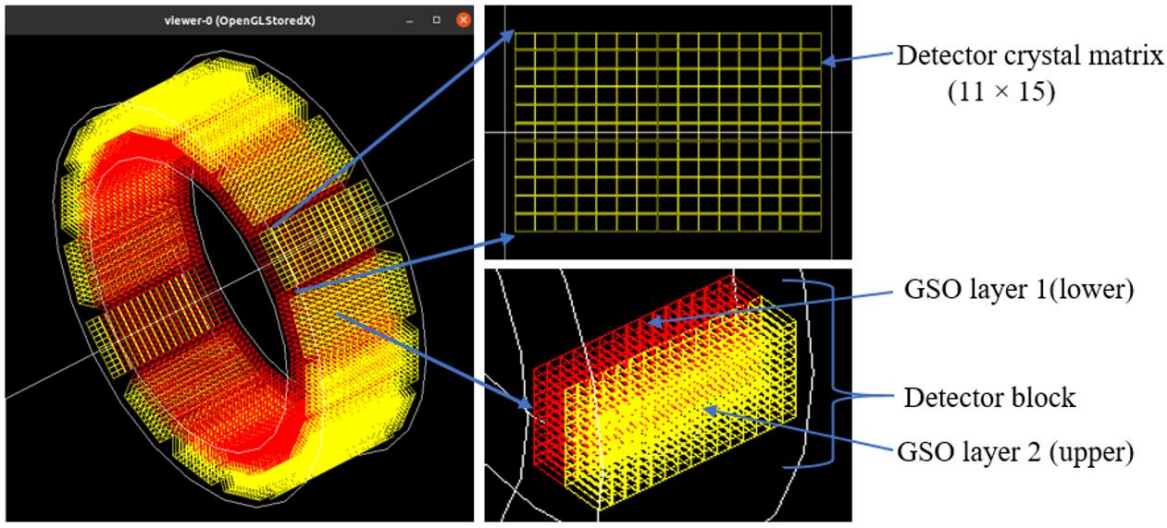

The physical processes are defined in the digitizer chain module. The digitizer chain module pre-processes the hits by sorting, summing (adder), and regrouping (readout) them to create single hits. The single hits were time-stamped and stored in the coincidence window set to 100 ns, with an offset value of 1000 ns. This 100 ns coincidence window was used to accommodate the 85 ns half life of the 5/2 intermediate state in the decaying process of ^{111}In [1, 8]. The GSO detector parameters used in the simulation include a temporal time resolution of 0.549 ns for a 2.9 mm GSO crystal (1.5% Ce) as recommended by Okumura et al. 2015 [21]. Additional parameters include an energy threshold of 1.0 keV and an upper limit of 1000 keV. The coincidence sorter, which selects singles that are coincident, is configured at the digitizer level in our simulation as shown in Figure 2.

Figure 2: Schematic diagram of the digitizer chain [23].

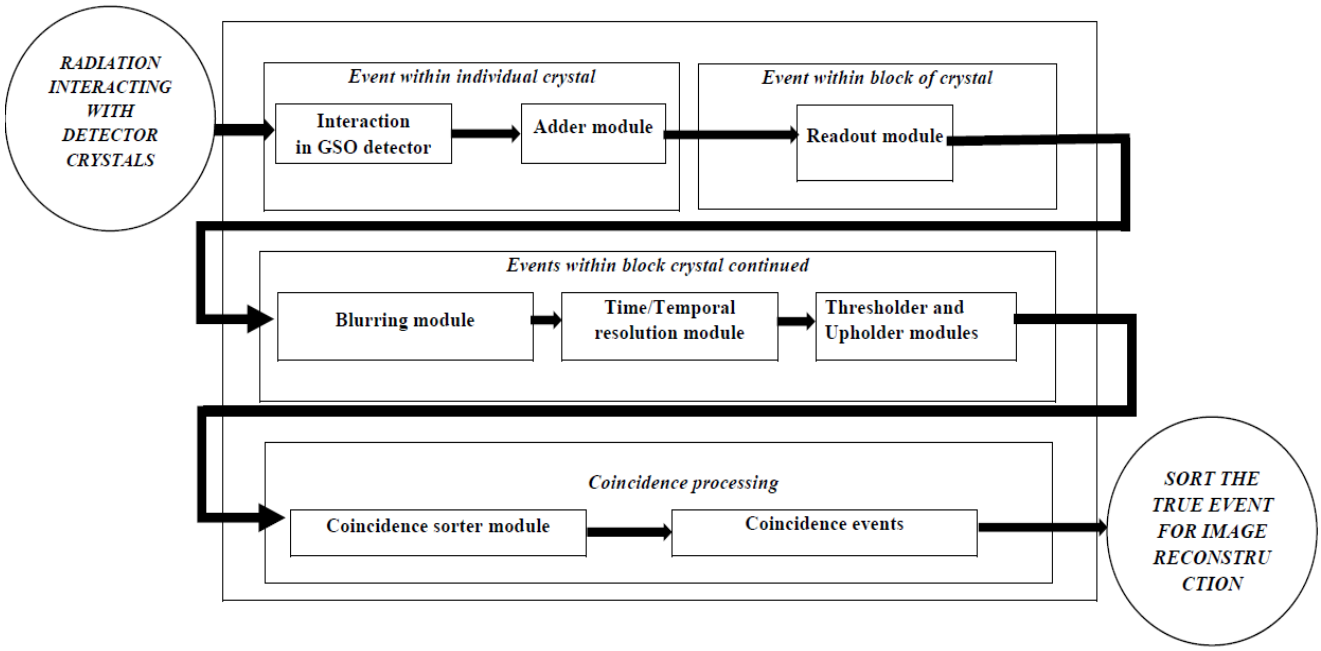

2.2. Collimator design and optimization

To design and optimize the collimator, GATE simulations of the RIKEN small animal PET scanner were performed as shown in Figure 1. This was followed by designing various collimator geometries and simulating a ^{111}In source to evaluate their effectiveness. The

outcomes of the GATE simulations were comprehensively analyzed using ROOT [24]. More details of the collimator design and optimization process are provided below.

2.2.1. Collimator design

A trapezoidal collimator block design was chosen to effectively utilize the geometry of the small animal PET detector. A singularly designed collimator block has 16.31 mm × 37.5 mm dimensions for the surface facing the crystals, and 12.33 mm × 37.5 mm for the surface facing the scanned object. The thickness of the collimator (hole length) is restricted to 10 mm to prevent overlapping of collimator blocks on their edges. An individual collimator block is equipped with 105 central full-sized rectangular parallel holes, as depicted in Figure 3.

Figure 3: A 3D picture of a trapezoidal collimator block with a 7 × 15 array of parallel rectangular holes.

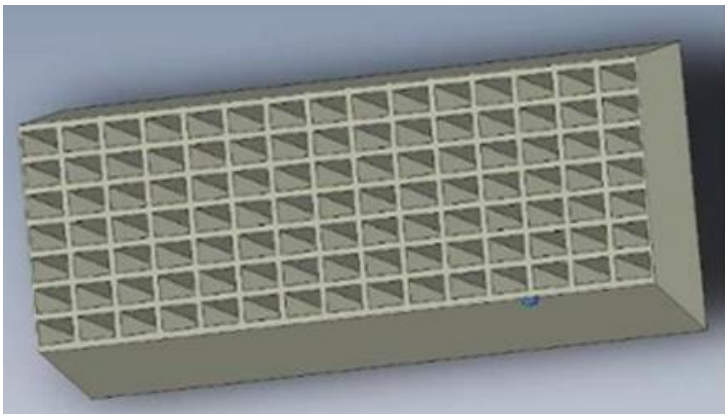

The trapezoidal collimator block design with rectangular parallel holes was chosen for the small animal PET detector for several reasons. The trapezoidal shape allows for efficient use of space, fitting more blocks compactly. The rectangular holes match the PET scanner's rectangular detector crystals, hence improving gamma ray direction. The final configuration of the collimator system consisted of sixteen (16) trapezoidal collimator blocks in a ring-like structure with an outer radius of 41.0 mm, as illustrated in Figure 4 (a & b). To allow collimator flexibility and protect the detector crystals from potential damage upon contact, the distance between detector and collimator was maintained to 6.5 mm [25, 26].

Figure 4: GATE simulation of the PET detector assembly with a collimator (in blue and white) attached, viewed; (a) in the transaxial (XY) plane, (b) at 45^0.

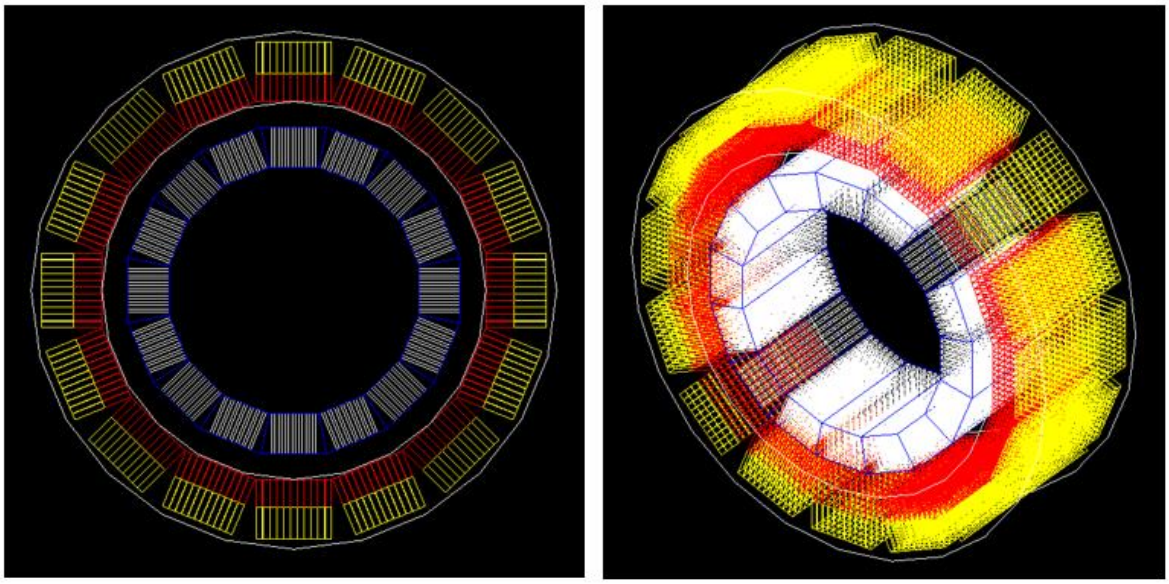

(a) (b)

In collimator design and optimization, it is essential to consider fixed, fundamental and adjustable collimator geometry parameters. Fixed collimator design parameters are dictated by the imaging system's physical characteristics and cannot be changed by the designer. These include the choice of radionuclide, the intrinsic resolution of the detector system and the distance between the collimator and the detector crystal [25, 26].

On the other hand, fundamental design parameters can be adjusted to enhance performance. They include the choice of collimator material (such as lead, tungsten, or gold) and the collimator geometry which covers the shape of collimator blocks, the specifications of hole axes, the arrangement of hole arrays, and the tapering of hole diameters. Adjustable collimator geometry parameters provide further opportunities for refinement. Key parameters in this category are collimator height or thickness (T), hole diameter (D) and hole separation (HOLSEP) which is the distance between the centers of adjacent holes [25, 26]. Therefore, by carefully adjusting these parameters, the collimator can be optimized to meet specific imaging requirements effectively.

For this study, pure tungsten was selected as the collimator material due to its significant advantages. These include the high density (approximately 19.3 g/cm^3) and atomic number (Z=74) which contribute to excellent attenuation of gamma rays [27]. These characteristics help to reduce the non-directional and scattering gamma rays resulting to enhanced image clarity. During the collimator designing work, two parameters, namely sensitivity and spatial resolution are typically used to assess performance [25, 26]. However, achieving higher sensitivity in parallel collimators often comes at the expense of spatial resolution, and vice versa. The collimator optimization described in this study is intended for small animal (e.g. rats and mice) imaging applications. Therefore, for accurate quantification of the sizes of imaged organs, the collimated imager must achieve higher spatial resolution [14].

In practice, the variation among parallel-hole collimators is confined to hole shape and the three geometrical dimensions (T, D and HOLSEP) that define the hole. In the process of collimator optimization, while balancing the trade-off between spatial resolution and sensitivity, collimator septa thicknesses were incremented from the initial setup of 0.2 mm by 0.2 mm to 1.2 mm. Considering the geometry of the RIKEN small animal PET detector, it is possible to extend septa thickness up to 1.3 mm. However, such an increase would lead to a substantial loss of geometric efficiency. As a result, only six collimator geometric designs, as outlined in Table 2, were simulated. After the simulation of these collimators, the ^{111}In source was modelled and the image reconstruction algorith was developed as explained in the proceeding sections.

Table 2: Selected collimator hole parameters for optimization

SEPTA THICKNESS	COLLIMATOR HOLE DIMENSIONS		
[MM]	LENGTH [MM]	WIDTH [MM]	HOLE AREA [MM^2]
0.2	2.3	1.5	3.45
0.4	2.1	1.3	2.73
0.6	1.9	1.1	2.09
0.8	1.7	0.9	1.53
1.0	1.5	0.7	1.05
1.2	1.3	0.5	0.65

2.2.2. Source modeling and simulation

In this study, a 0.25 mm radius, 1.0 MBq ^{111}In source was simulated. The complete radioactive decay of the ^{111}In source, which includes the emission of 171.3 keV and 245.4 keV gamma rays, as well as an intermediate half-life of 85 ns [1, 6, 8, 28-31], was simulated.

2.2.3. Image reconstruction algorithm

The fundamental principle underlying the image reconstruction algorithm is based on a pair of collimated detectors measuring two cascade gamma rays in coincidence [1, 8]. For each coincidence event, two projections (in red) emanate from the hit detectors, passing through the collimator holes as shown in Figure 5.

Figure 5: Illustration of image reconstruction procedure. The black dashed lines emitted from the source to P_1 and P_2 (interaction position on a detector) represent the 171 keV and 245 keV gamma rays, respectively.

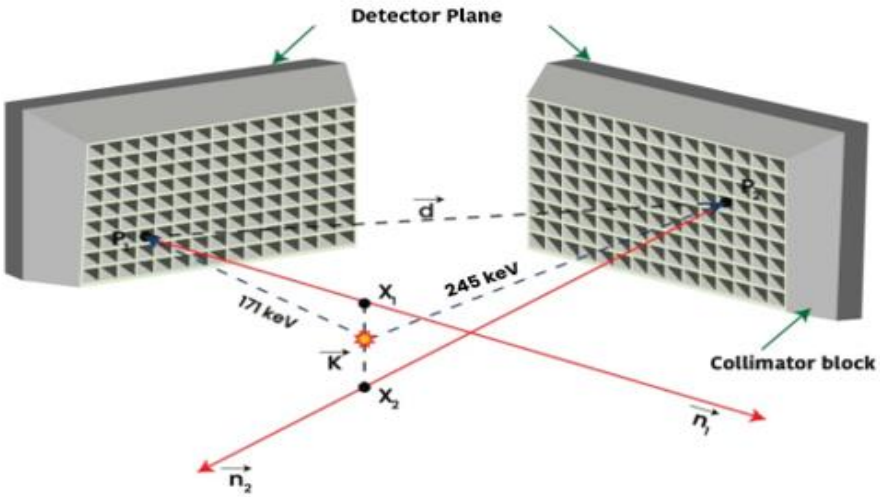

As depicted in Figure 5, if the two backprojected lines are not parallel (indicating they do not originate from detector crystals with parallel collimation), the point of intersection between these lines establishes the exact location of the decaying vertex of the nucleus. The identified decay vertex (emission point) is almost completely free from any interference of other emitted gamma rays reaching the detector crystals, unlike conventional SPECT [21]. Therefore, to reconstruct a 3D vertex of an individual decaying nucleus, the acquired list-

mode data from the GATE simulation goes through three main functions, namely, a) selection of gamma-ray pair, b) determination of interaction position, and c) determination of 3D vertices of an individual decaying nucleus and bin them into image voxels. A flowchart detailing the algorithm developed in ROOT software is shown in Figure 6.

Figure 6: Flowchart of the 3D vertex reconstruction algorithm developed in the ROOT CERN framework

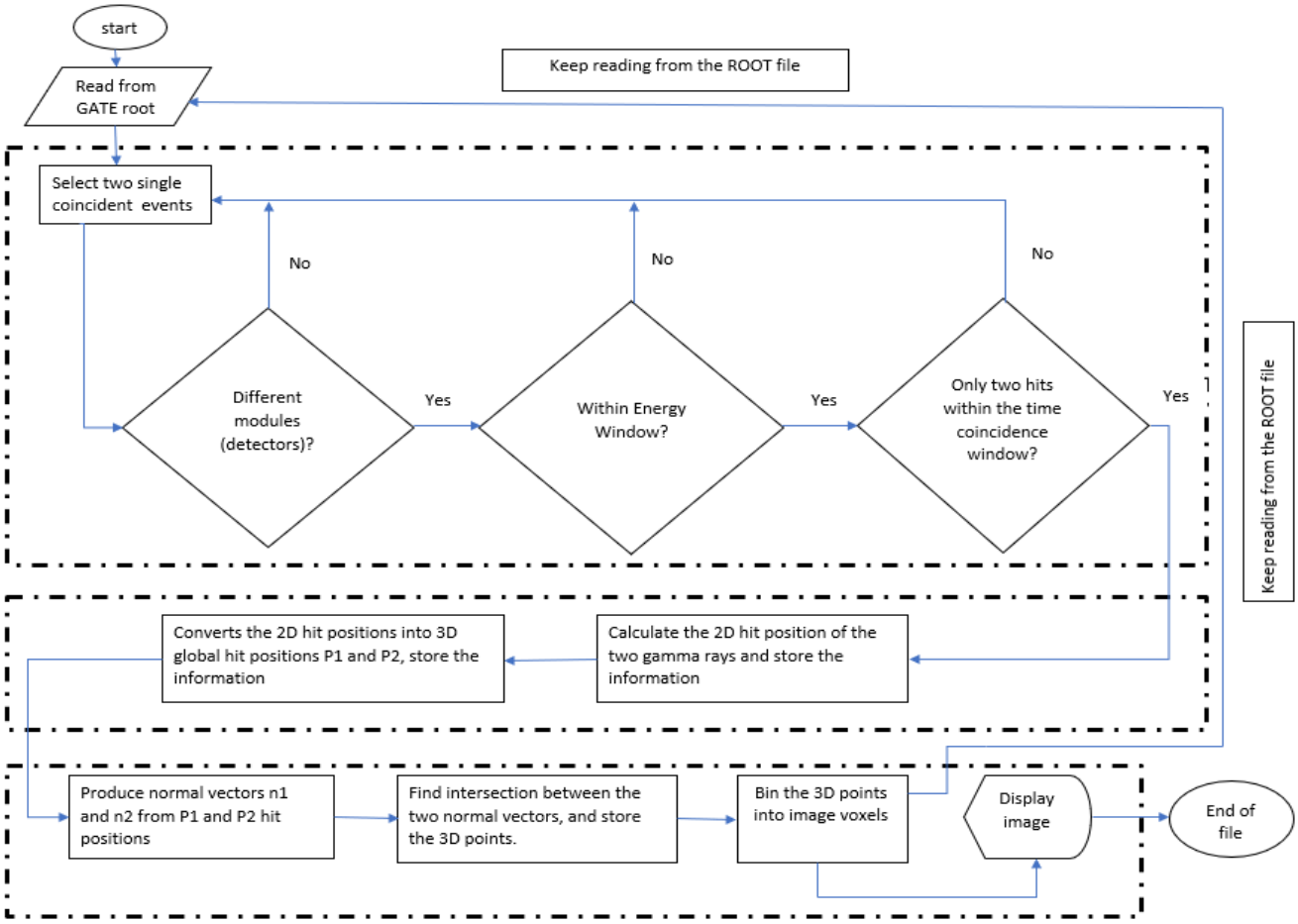

a) Selection of gamma-ray pair

The algorithm reads from the GATE-ROOT file and selects pairs of gamma-rays (singles), γ_1 and γ_2, which satisfy the following criteria: (1) the two registered singles, from γ_1 and γ_2, were recorded in coincidence in two different non-collinear detector crystals (which are from different detector modules). (2) The energies, E_1 and E_2 of the two singles are 171.3 keV and 245.4 keV. However, to filter out scattered photons, especially those arising from

the collimators and phantom, the energy window is set to ± 15%. In this case, the algorithm will only accept gamma-ray energies of 171.3 keV ± 15% and 245.4 keV ± 15%. Lastly, (3) the two singles must be detected within a set time coincidence window (100 ns for this study). Only events that meet these criteria were recorded as valid coincident events.

b) Determination of interaction position

In part (a), the filtered coincidence events were used in the image reconstruction algorithm. The algorithm determines the 2D position (x, y) of a hit detector based on its crystalID and moduleID. It then converts the 2D local interaction positions (x1, y1) and (x2, y2) into 3D interaction positions, labeled as $q(x, y, z)$ and $n(x, y, z)$. Since these 3D points correspond to the origin of the global coordinate system, we assume the detector module is at this origin. The coordinates are then translated by 47.5 mm along the x-axis, which is the radius of the ring detector. Next, the translated coordinates are rotated around the z-axis ($R_z(\theta)$) using an angle (θ) calculated from Equation 01. This gives the final 3D global interaction positions, denoted as $P_1(x, y, z)$ and $P_2(x, y, z)$. Only the gamma-ray pairs meeting these criteria are stored.

$$\theta = \frac{ModuleID}{Number\ of\ Modules} \tag{01}$$

c) Determination of 3D vertices of an individual decaying nucleus and bin into image voxels

At the end of the second function described in part (b), global interaction positions $P_1(x, y, z)$ and $P_2(x, y, z)$ for each coincidence event are known. Therefore, in the third function, normal vectors $\vec{n}_1(x, y, z)$ and $\vec{n}_2(x, y, z)$, called collimator projections, which are perpendicular to each detector crystal plane, are projected from $P_1(x, y, z)$ and $P_2(x, y, z)$, towards the center of FoV to locate the probable source emission position as shown with red lines in Figure 5. These normal vectors are determined using the angular position of a

respective detector plane, as shown in Equation 02. The negative sign indicates that the normal vectors are pointing towards the center of FoV (inwards).

$$\vec{n}(x, y, z) = (-cos\theta, -sin\theta, 0) \quad (02)$$

The normal vectors usually go to infinity, to determine their finiteness, a scalar quantity S is multiplied with the normal vector ($\vec{n}$), and a new line named L is formed. The clear definition of line L_i from Figure 5 is: $X_i - P_i = (\vec{n}_i S_i)$. By making X_i the subject, we get equation 03 as shown below. Where i = 1 or 2, other parameters have been defined already.

$$X_i = P_i + (\vec{n}_i S_i) \quad (03)$$

Here we are interested with vector $\vec{k}$ given in Figure 5, which is defined by two points, X_1 and X_2. We define vector $\vec{d}$ as the difference between the points P_1 and P_2 on each detector face. Therefore, through analysis of the triangles $\Delta X_1P_1P_2$ and $\Delta X_2X_1P_2$ in Figure 5, the vector $\vec{k}$ is given by Equation 04.

$$\vec{k} = (\vec{n}_2 S_2) - (\vec{n}_1 S_1) + \vec{d} \quad (04)$$

Note that, a vector $\vec{k}$ is orthogonal to both $\vec{n}_1$ and $\vec{n}_2$, therefore, taking a dot product with $\vec{n}_1$ and $\vec{n}_2$, both equations will result in zero as shown in Equations (05) and (06). In those equations, all the parameters are known except S_1 and S_2. Therefore, by solving a system of simultaneous equations, we obtain the values of S_1 and S_2 and substitute them into equation 03, and then the X_i are found.

$$(\vec{n}_1 \cdot \vec{n}_2) \times S_2 - (\vec{n}_1 \cdot \vec{n}_1) \times S_1 + \vec{n}_1 \cdot \vec{d} = 0 \quad (05)$$

$$(\vec{n}_2 \cdot \vec{n}_2) \times S_2 - (\vec{n}_2 \cdot \vec{n}_1) \times S_1 + \vec{n}_2 \cdot \vec{d} = 0 \quad (06)$$

The decay vertex, which is a 3D point, is then determined as the intersection point between, or a mid-point of the shortest segment between two (L_1 and L_2) projected lines (collimator projections), which is given as the arithmetic mean of X_1 and X_2. Finally, the

calculated 3D decay vertices are binned into voxels. These voxels represent small volumes depicting the radioisotope distribution. Ultimately, all these voxels are binned together to reconstruct the entire image, showing the radioactivity distribution in the scanned object. After having all six collimator designs and developed a custom image reconstruction algorithm, the next steps involved evaluating the collimators and reconstructing images from each one.

2.2.4. Collimator designs and their preliminary reconstructed images

a) Collimator evaluation

This study evaluated collimator designs based on energy spectra quality, energy resolution, sensitivity and spatial resolution. For energy spectra and resolution analyses, the source was placed at the center of FoV in two scenarios. The first scenario involved a detector guided by the collimators of varying septa thickness and the other scenario involved a detector without collimators. Data for each simulation were obtained using 100 s acquisition time. Detected energies were extracted using time coincidence and energy windows as described in the preceeding sections of this paper [1, 8]. The energy spectra were generated using histograms with N equal bins covering the energy range from E_{min} to E_{max}. The spectrum from the uncollimated detector served as a reference, and the energy window was applied to ensure smooth spectra for collimated detectors [1].

In the digitizer chain module (electronic read-out simulator) given in Figure 2, the blurring module simulates Gaussian blurring of the energy spectrum. Usually, this is accomplished by introducing a resolution, R_0 (FWHM), based on the detector crystal in use (e.g. GSO), at a given energy of reference, E_0 [32]. In this study, R_0 (FWHM) is 10% [33], while E_0 is 171.3 keV and 245.4 keV for 171.3 ±15% keV and 245.4 ±15% keV, respectively. Therefore, after a series of simulations, the energy resolution (E_{res}) for each energy peak was estimated by determining the full width at half maximum (FWHM) of each energy photopeak, then dividing it by the centroid energy E_0, and expressing the result in percentage.

To evaluate collimator sensitivity and spatial resolution, a 0.25 mm radius, 1.0 MBq ^{111}In source was simulated for 100 seconds in all six collimator designs. Sensitivity and spatial resolution were determined using valid coincidence events filtered by energy window for scattered events and time window for random events [1, 8, 17]. Finally, collimator sensitivity was defined as the number of valid coincidence counts passing through the collimator per second per Becquerel (cps/MBq) [25, 26]. Equation 07 was used to calculate sensitivity for each collimator design.

$$\text{Sensitivity}(S) = \left(\frac{\text{Number of valid coincidence counts per second (cps)}}{\text{Source strength (MBq)}} \right) \quad (07)$$

For adjustable collimator parameters, a simple method estimates geometric resolution (Rg). The Rg can be calculated using Equation 08. The ratio D/T is essential for estimating resolution and represents the tangent of the collimator hole's opening angle, known as the acceptance angle. Here, D refers to the hole diameter or size for other shapes (see Table 2), T is the hole length or collimator thickness, set at 10.0 mm for this study, z is the distance from the source to the detector crystal. In this study, z is 47.5 mm.

$$R_g = \left(\frac{D}{T} \right) \times z \quad (08)$$

The spatial resolution ($FWHM_{col}$) of the collimator can be estimated analytically using Equation 09 [25, 26]. The sigma (σ) value is derived from the Gaussian fit applied to the point spread function (PSF) obtained from a reconstructed image of a simulated source.

$$FWHM_{col} = 2\sqrt{2\ln 2} \times \left(\frac{D}{T} \right) \times z = 2.35482 \times \sigma \quad (09)$$

For parallel holes, Rg reliably estimates analytical spatial resolution in terms of $FWHM_{col}$, with the relationship that $R_g \leq FWHM_{col} \leq 2R_g$ under optimal collimator

conditions [25]. Therefore, in this study, the collimator design demonstrating optimal spatial resolution (FWHM) and promising sensitivity was chosen for further investigation.

b) Preliminary images from all six collimator designs

Simulated files for all six collimator configurations were further analyzed, and 2D flattened images were generated from the 3D reconstructed emission positions. Using the energy and time coincidence windows described into this paper, transaxial (XY) 2D flattened images integrated over Z and their corresponding 1D projections were reconstructed using valid coincidence events [17]. The reconstructed 2D flattened images revealed the optimal collimator.

2.3. Determination of the field of view of the collimated imager

Two tests were performed with ^{111}In source for the determination of the FoV. The first test was to assess the FoV using the coincidence detection efficiency values, and the second test was to assess the FoV using the accuracy of reconstructed source emission positions. To determine the coincidence efficiency, a 1.0 MBq ^{111}In source with a 0.25 mm radius was simulated at the center of FoV for an acquisition time of 100 s. Then the source was moved off-center in 1.0 mm steps in both axial and transaxial directions. The coincidence detection efficiency values were calculated using Equation 10.

$$\text{Coinc. det. eff.} = \frac{\text{Number of valid coinc. counts}}{\text{Source strength (MBq)} \times \text{Acquisitiontime (s)}} \tag{10}$$

In the second test, the proposed imaging system was tested on its ability and accuracy in reconstructing a source emission position along the y axis (same as x axis) and z axis. To perform this test, a 0.25 mm radius, 1.0 MBq ^{111}In source was simulated as for coincidence detection efficiency determination. The x, y, and z collimator projection data acquired from simulation were utilized to create a point spread function (PSF) for the source. For each coordinate axis, a Gaussian fit function was applied to a PSF of the acquired collimator projections along the x, y and z axes. After Gaussian fitting, the obtained peak centroid, μ,

corresponds to the probable source location, with the standard deviation (σ) representing the uncertainty in position reconstruction. Therefore, a single reconstructed source position is expressed as $\mu \pm \sigma$ (mm).

In conclusion, for coincidence detection efficiencies, the obtained values were plotted into a curve and analysed. On the other hand, for source emission position reconstruction accuracy, the estimated peak centroid positions, denoted as μ (mean reconstructed positions), were compared to the true simulated source positions using graphs to demarcate the FoV. Thus, the region extending from the center of the collimated small animal PET scanner in axial or transaxial directions, where the coincidence detection efficiencies are constant and the peak centroid positions, μ, are almost the same as actual simulated source positions, was termed as the FoV of the simulated imaging system.

3. RESULTS AND DISCUSSIONS

3.1. Collimator designs and their preliminary reconstructed images

a) Evaluation of six collimator designs

For the assessment of quality of energy spectra and resolution, the energy spectrum for the ^{111}In point source obtained without a collimator, as depicted in Figure 7, served as the reference standard. The Compton edge for each energy peak is indicated by the two bumps on the far left of the energy spectrum. The Compton edges have energies of approximately ~69 keV for 171.3 keV and ~120 keV for 245.4 keV, respectively. The calculated energy resolution for each photopeak in Figure 7 was 8.70% and 10.31% for 171.3 keV and 245.4 keV, respectively.

Figure 7: Energy spectrum of simulated ^{111}In point source acquired through uncollimated GSO detectors.

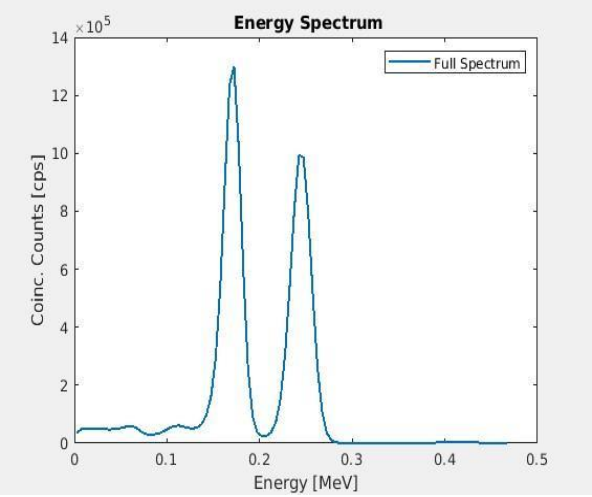

In contrast to the spectra obtained with collimated GSO detectors (Figure 8), the spectrum without collimators is smooth and free of scatters (Figure 7). This indicates that the scattered peaks in the spectra acquired from collimated GSO detectors, as illustrated in Figure 8 (a-f), are directly influenced by the attached collimators. Scatters typically introduce blurring in images; therefore, in medical imaging, efforts are made to remove them either before or after image reconstruction. Using the energy window described in this paper, smooth energy spectra (in red) for the collimated detectors (Figure 8a-f) were obtained.

However, the only invalid (false) events that might appear in the reconstructed images are either due to inter-crystal scatters or septa-penetrated events. Both inter-crystal scatters and septa-penetrated events are known to introduce blurring in reconstructed images and degrade image resolution [34]. The estimated energy resolution values for smoothed photo peaks ranged from 8.70% to 8.96% for 171.3 keV, and 6.06% to 10.31% for 245.4 keV, respectively. This indicates that all computed energy resolutions closely aligned with the true simulated energy resolution of 10%, suggesting that the simulated GSO detectors effectively mimic real GSO detectors in their interactions with photons.

Figure 8: Energy spectra of simulated ^{111}In point source acquired through various collimator septa thicknesses.

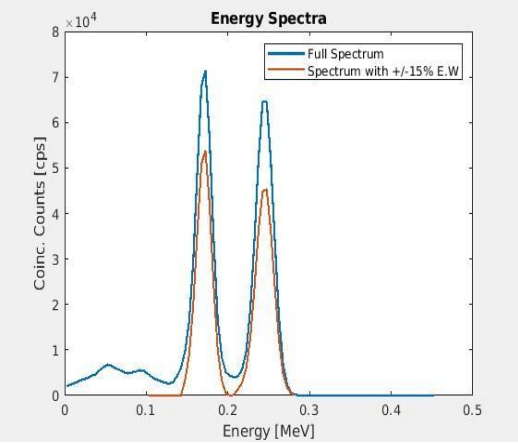

(a) Spectra for 0.2 mm septa

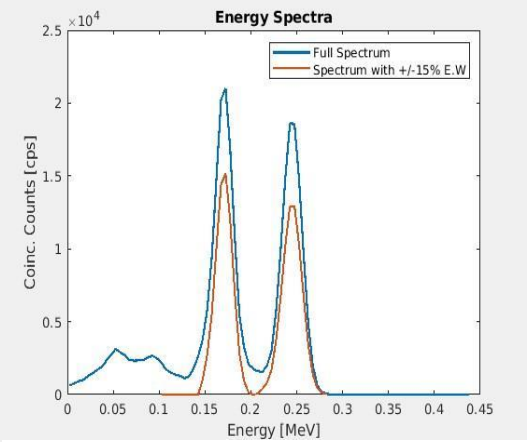

(b) Spectra for 0.4 mm septa

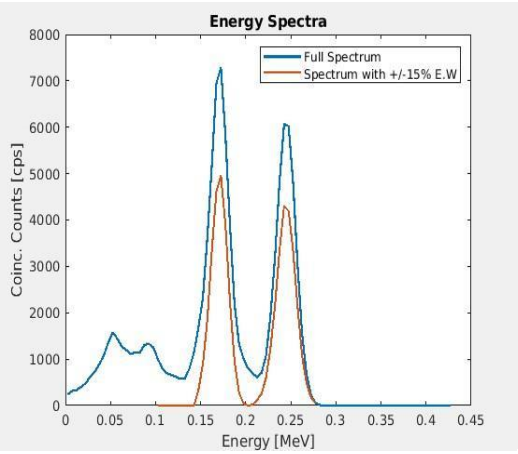

(c) Spectra for 0.6 mm septa

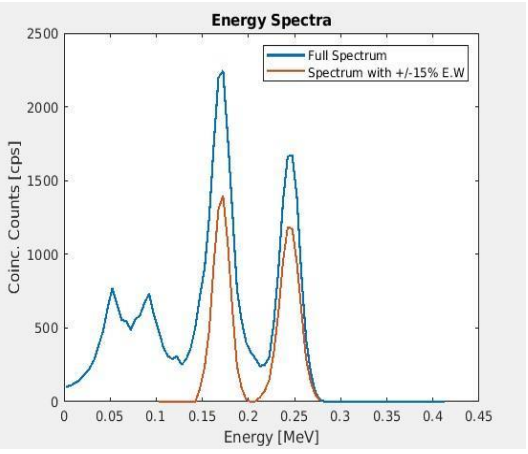

(d) Spectra for 0.8 mm septa

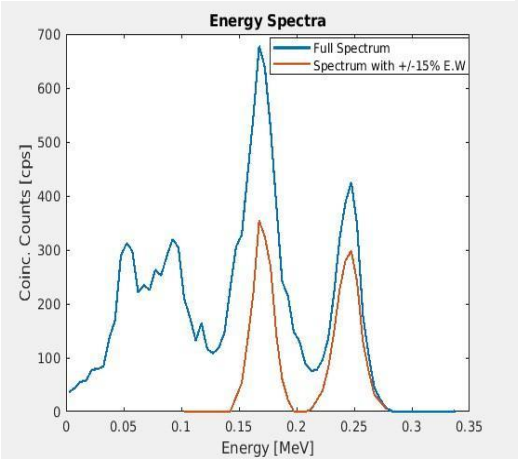

(e) Spectra for 1.0 mm septa

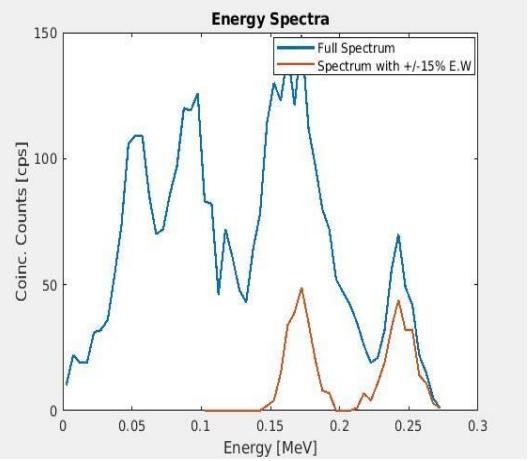

(f) Spectra for 1.2 mm septa

Despite achieving good energy resolution with 1.2 mm collimator septa, the poor full energy spectrum, resulting from the absorption and/or blocking of many geometric photons from reaching the detector crystal, disqualifies the collimator design with 1.2 mm septa thickness. However, other collimator designs have demonstrated promising energy spectra as well as energy resolutions.

In addition to evaluating the quality of energy spectra and estimating energy resolution, we also determined the sensitivity (cps/MBq). As shown in Figure 9, as expected, the sensitivity decreased with an increase in the thickness of the collimator septa.

Figure 9: Sensitivity (cps/MBq) against septal thickness (mm).

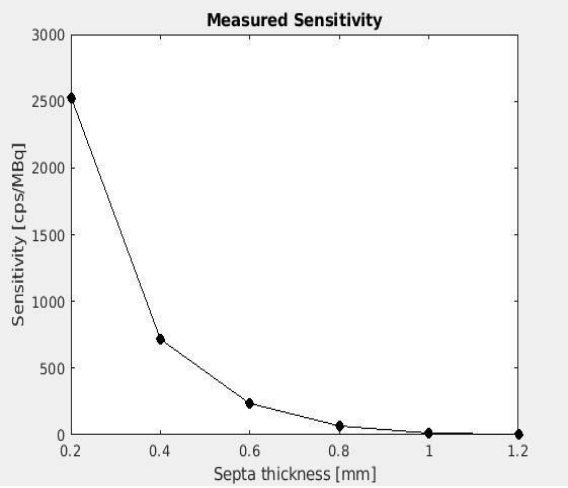

The decrease in sensitivity can be directly attributed to the reduced geometrical acceptance. However, the decline in sensitivity significantly contributes to the enhancement of spatial resolution (FWHM) in the imaging system. Yet, this loss of sensitivity due to physical collimation is more than compensated for by the capabilities of the image reconstruction algorithm. This algorithm is such that every identified valid coincidence event pinpoints the 3D vertex of an individual decayed nucleus, forming a distinct image point [17], a capability not possible in standard PET and SPECT imaging systems [6-9].

Following the description of sensitivity was the description and analysis of spatial resolution. In this study, two resolutions, namely geometrical resolution (Rg) and measured

resolution (FWHM), were quantified and analyzed. As shown in Figure 10 (a & b), both the geometrical resolution (Rg) and measured spatial resolution (FWHM) values decrease (improve) as the septa thickness is increased. The improvement is directly related to the non-directional and penetrated photons being stopped or absorbed by the collimator septa, thereby narrowing the width of the point spread function (PSF) of a source.

Figure 10: Spatial resolution; (a) transaxial, and (b) axial resolution

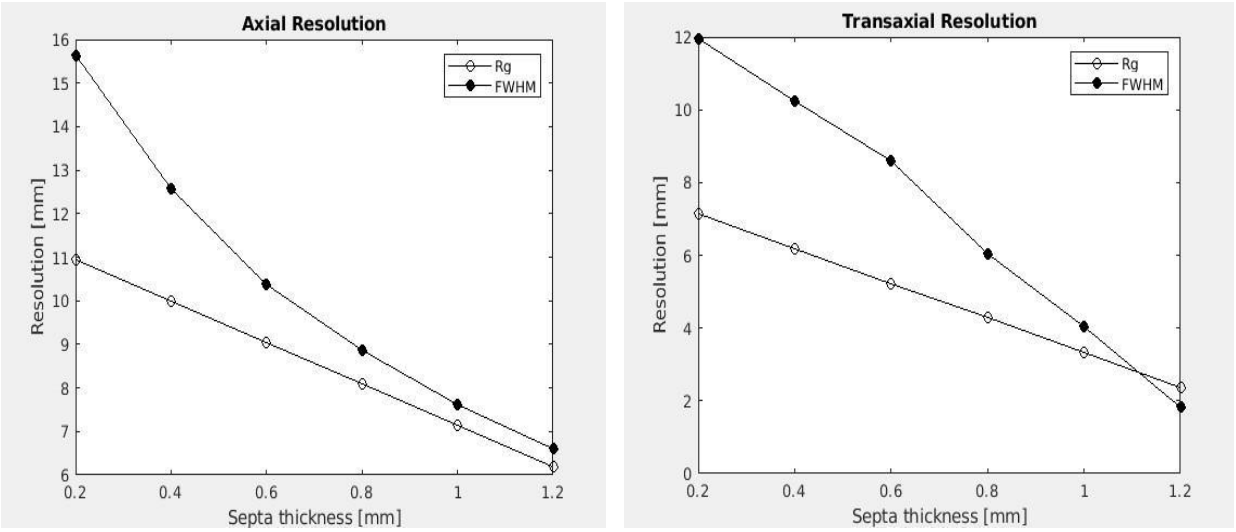

(a) (b)

According to Gunter [25], Rg is related to FWHM with the inequality: $Rg \leq FWHM_{col} \leq 2Rg$. As shown in Figure 10 (a & b), all the collimators adhered to the inequality except the 1.2 mm septa collimator for transaxial resolution with Rg = 2.38 mm and FWHM = 1.85 mm. Thus, the 1.2 mm septa collimator was disqualified [25]. It follows that, the optimal design arises as the 1.0 mm collimator septa, paired with parallel rectangular hole sizes of 1.5 mm × 0.7 mm, surpasses the other collimator configurations presented in this study by having better spatial resolution (FWHM). However, the axial spatial resolution value of 7.6 mm FWHM in this study was poorer compared to the spatial resolutions of 7.0 mm and 6.7 mm FWHM reported by Liu et al [35] for simulated and prototype cascade gamma ray imagers [35]. Nonetheless, the transaxial resolution of 4.1 mm FWHM from this study was superior to those presented by Liu et al. [35].

b) Preliminary imaging results

As depicted in Figure 11 the transaxial (XY) view of reconstructed 2D flattened images integrated over Z reveals that the size of an image decreases each time the collimator septa are incremented by a factor of 0.2 mm.

Figure 11: The 2D transaxial (XY) view of reconstructed flattened images (integrated over Z) and their corresponding 1D X-projections of a simulated point source acquired with varied collimator septa.

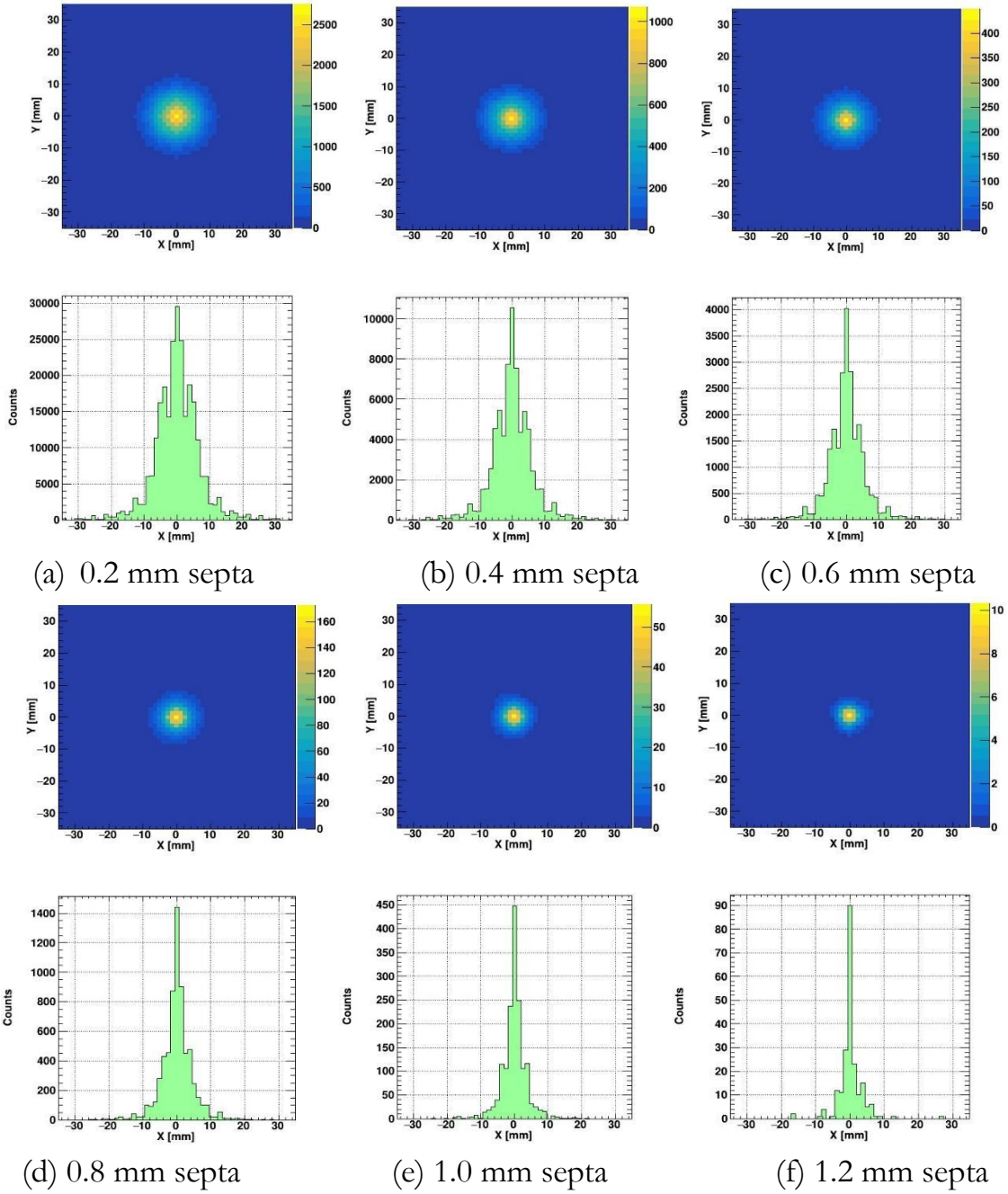

(a) 0.2 mm septa (b) 0.4 mm septa (c) 0.6 mm septa

(d) 0.8 mm septa (e) 1.0 mm septa (f) 1.2 mm septa

The decrease in the size of the 2D reconstructed image is also evident from the analysis of the 1D X-projections, as shown in Figure 11. With each increment in collimator septa thickness, a finer image is produced. The reduction in image sizes is directly linked to the narrowing of the point spread function (PSF) with each increment in collimator septa.

Upon comparing the reconstructed images in Figures 11 (a to f), despite the lower image sensitivities of about 16.02 cps/MBq and 2.13 cps/MBq (Figure 9), the images presented in Figure 11 (e) and Figure 11 (f) exhibit less noise and better spatial resolution (FWHM). The spatial resolutions of the two collimators used to generate the images in Figures 11 (e) and 11 (f) are as follows: 4.13 mm FWHM (transaxial), 7.61 mm FWHM (axial) for the 1.0 mm collimator septa, and 1.85 mm FWHM (transaxial), 6.61 mm FWHM (axial) for the 1.2 mm collimator septa. However, the collimator geometry that generated the image in Figure 11 (f) has been disqualified, as some of its analytical (FWHM) and calculated (Rg) resolution values do not adhere to the inequality $Rg \leq FWHMcol \leq 2Rg$, as suggested by Gunter [25, 26]. Therefore, the findings from this study continue to cement that the 1.0 mm collimator septa, coupled with parallel rectangular hole sizes of 1.5 mm × 0.7 mm, is the best option for our prototype.

3.2. The FoV of the cascade gamma-ray coincidence (CGC) imager

The determined FoV through coincidence cofficiencies values and accuracy of emission reconstruction positions is presented and discussed. In this study, the FoV is termed as the region from the center of the CGC scanner where the valid coincidence detection efficiency is almost constant and where the reconstructed source emission positions are closer to the true simulated source positions. Thus, for a 0.25 mm radius, 1.0 MBq ^{111}In source simulated at the center of the CGC scanner, a total of 1602 valid coincidence events were acquired, giving about 1.602×10^{-5} as the coincidence detection efficiency. As shown in Figure 12, the coincidence detection efficiencies off-center in 1.0 mm steps in transaxial (source-to-detector) and axial directions were computed, respectively.

Figure 12: Coincidence detection efficiency against source displacement in (a) transaxial direction and (b) axial direction.

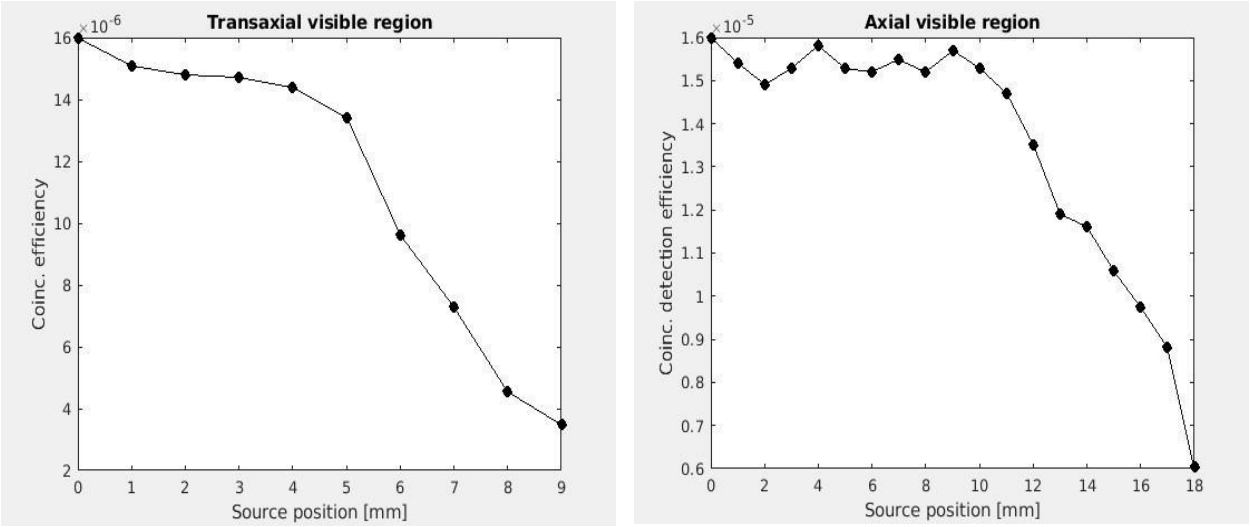

(a) (b)

Results show that the coincidence efficiencies value of ~ 1.47×10^{-5} extends from the center of the CGC scanner to a distance of 4.0 mm in both ends. However, the coincidence detection efficiency can be tolerated to a distance of 5.0 mm, where a coincidence detection efficiency value is about 1.34×10^{-5} (Figure 12(a)). The coincidence detection efficiency value then drops gradually as the transaxial displacement continues. On the other hand, the coincidence detection efficiency off-center in 1.0 mm steps in axial direction was also computed. Results show that a constant coincidence detection efficiency value of ~ 1.48×10^{-5} extends from the center of the FoV to about 11.0 mm at both ends.

The coincidence detection efficiency value can be tolerated to about 12.0 mm, where a coincidence efficiency was about 1.35×10^{-5} (Figure 12(b)). Beyond that, the coincidence detection efficiency value starts to drop gradually as the axial displacement increases. Apart from using coincidence efficiency, reconstructed source emission position accuracy was used to determine the FoV (visible region). As shown in Figure 13, results show that the simulated CGC imaging system can reconstruct the emission positions in transaxial direction (y-axis) and axial direction closer to the simulated true source position.

Figure 13: Reconstructed source positions (a) y positions vs. the true simulated y positions and (b) z positions vs. the true simulated z positions

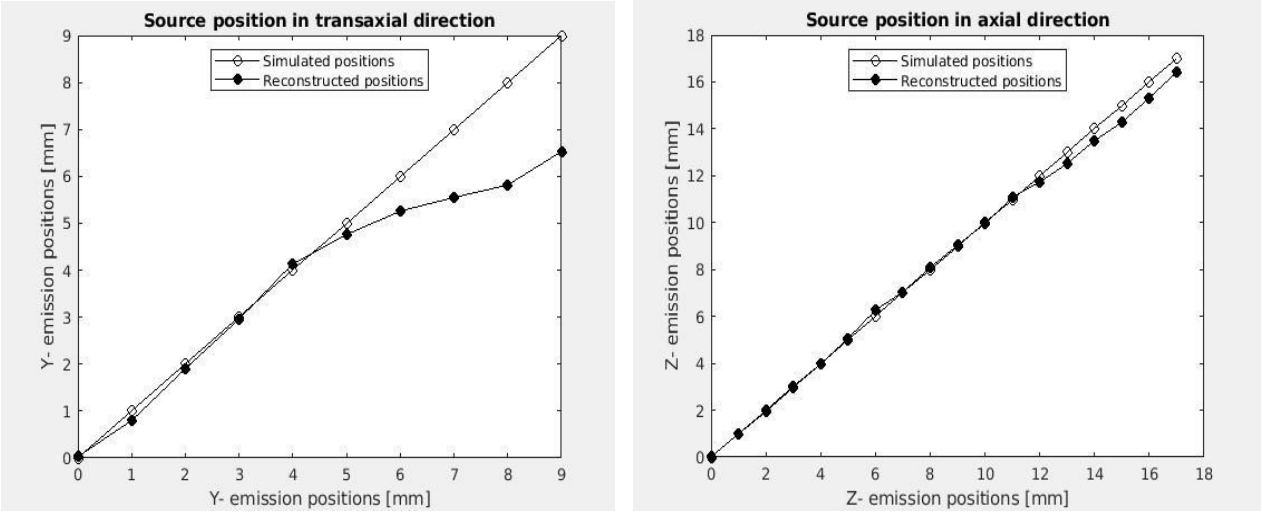

(a) (b)

The simulated CGC imaging system can reconstruct the source emission positions closer to the true simulated source positions as shown in Figures 13. However, this capability is only valid within a region that extends from the center of the CGC scanner to about 5.0 mm and 12.0 mm in both ends in transaxial and axial directions, respectively. It has been noted that at 5.0 mm and 12.0 mm in both ends in transaxial and axial directions, the mean reconstructed source positions (μ) are 4.8 mm and 11.7 mm, respectively. Thus, above these points, the deviation between reconstructed and true source positions is much bigger as shown in Figure 13. However, in both axial and transaxial directions, the position reconstruction uncertainties (± σ) were neglected as they are very small with a magnitude of approximately 10^{-3}.

By looking at Figure 12 (a & b), one will notice that for point sources simulated above 5.0 mm in transaxial direction or above 12.0 mm in axial direction, their coincidence efficiencies are very low. This causes the reconstruction of mean positions (μ) to deviate significantly from the simulated source positions, as can be seen in Figures 13. The reasons for the discrepancy might be due to poor sampling of coincidence events. Therefore, this indicates that the designed collimator [18], limits the original FoV.

4. CONCLUSIONS

In the current study, the design and optimization of collimator for cascade gamma-ray imaging has been implemented through GATE simulation platform. Six collimator designs were identified, evaluated and one collimator was selected. The selected collimator outperforms others by providing a good-quality reconstructed image (see Figure 11(e)) and achieving spatial resolutions of 7.6 mm FWHM for the axial direction and 4.1 mm FWHM for the transaxial direction. This collimator presents a viable solution for imaging internal organs larger than 7.6 mm, such as the brain, which typically has linear dimensions of approximately 12.0 mm for mice and around 8.0 mm for rats [36]. Despite the short acquisition time of 100 s used during the simulations, the selected collimator provides smoothed energy spectra of good quality and offers excellent energy resolution compared to other simulated collimator designs. Therefore, to obtain sufficient statistics in future studies, it is recommended that the simulation acquisition time be increased to around 900 seconds or more.

In this study, it has been revealed that the region that extends from the center of the CGC scanner to 5.0 mm in both ends of the transaxial and from the center of the CGC scanner to 12.0 mm in both ends of the axial direction is characterized by almost a constant coincidence detection efficiency value of ~1.47×10^{-5}. Therefore, it is concluded that, this region is the FoV of the proposed non-collinear CGC medical imaging modality. Within the determined FoV, the proposed non-collinear CGC imaging system with its custom image reconstruction algorithm can reconstruct mean positions (μ) ranging from 81.1% to 100% of the true simulated source positions.

ACKNOWLEDGMENT

We thank Prof. Chary Rangacharyulu from the University of Saskatchewan, Canada for welcoming us into the medical imaging group and assisting with collimator geometry. We

also thank Ms. Kaylyn Olshanoski from the University of Saskatchewan, Canada for her help in setting collimator geomerty. Prof. Fukuchi Tomonori is also acknowledged for providing us the parameters of the small animal PET scanner of RIKEN for simulation purposes. Additionally, we thank Prof. K. Vijay Sai from the Sri Sathya Sai Institute of Higher Learning, Vidyagiri Prasanthi Nilayam - India, for his time and expertise in this study.

FUNDING

Nkuba, L.L. acknowledges the financial support from the Tanzania Atomic Energy Commission (TAEC).

CONFLICT OF INTEREST

We have no conflicts of interest to disclose.

REFERENCES

[1] PAHLKA, R.B,; KAPPADATH, S.C,; MAWLAWI, O.R. A Monte Carlo simulation of coincidence detection and imaging of gamma-ray cascades with a scintillation camera. **Biomed. Phys. Eng. Express**, 4: 055012, 2018.

[2] SAFFER, J.R,; BARRETT, H.H,; BARBER, H.B,; WOOLFENDEN, J.M. Surgical probe design for a coincidence imaging system without a collimator. **Image Vis. Comput**, 511 LNCS, p. 333–341, 1992.

[3] BUTZ, T. Nuclear quadrupole interactions studied by time differential perturbed angular correlations of γ-rays. **Zeitschrift fur Naturforsch. - Sect. A J. Phys. Sci**, v. **51**, p. 396–410, 1996.

[4] HEMMINGSEN, L,; SAS, K.N,; DANIELSEN, E. Biological Applications of Perturbed Angular Correlations of γ-Ray Spectroscopy. **Chem. Rev**, v. 104, p. 4027–4061, 2004.

[5] CHIANG, C.C,; CHUANG, C.C,; NI, Y.C,; JAN, M.L,; CHUANG, K.S,; LIN, H.H. Time of flight dual photon emission computed tomography. **Sci. Rep**, v. 10, p. 1–13, 2020.

[6] UENOMACHI, M,; SHIMAZOE, K,; OGANE, K,; TAKAHASHI, H. Simultaneous multi-nuclide imaging via double-photon coincidence method with parallel hole collimators. **Sci. Rep***,* v. 11:13330, 2021.

[7] RANGACHARYULU, C,; LAI, THI KHANH. L,; OLSHANOSKI, K,; SANTOSH, S,; NKUBA, L.L,; FUKUCHI, T,; FUKUDA, M,; KANDA, H,; MSAKI, P.K,; SAI, K.V,; TAKAHASHI, N. Development of a Nuclear Gamma Cascade Correlations Based Medical Imaging System - A Novel Modality with Potentials for Replacement of SPECT and PET. International Conference on Clinical PET-CT and Molecular Imaging in the Era of Theranostics (IPET), **Book of Abstract-IPT 2020**, IAEA-CN-285/110, 2021.

[8] SHIMAZOE, K,; UENOMACHI, M,; MIZUMACHI, Y,; TAKAHASHI, H,; MASAO, Y,; SHOJI, Y,; KAMADA, K,; YOSHIKAWA, A. Double Photon Emission Coincidence Imaging using GAGG-SiPM pixel detectors. **J. Instrum***,* v. 12 C12055, 2017.

[9] SANTHOSH, R.S,; SHYAM, D.S,; FUKUCHI, T,; RANGACHARYULU, C,; VENKATARAMANIAH, K,; SAI, K.V. Design and Optimization of a Collimator for a New PET system using GATE simulation. *In*: PROCEEDINGS, 64TH DAE BRNS SYMPOSIUM ON NUCLEAR PHYSICS, 2019 Lucknow (Uttar Pradesh), India, p. 852-853, 2019.

[10] BRADY, E,; DEUTSCH, M. The angular correlation of successive gamma-rays. **Phys. Rev**, v. 78, p. 558–566, 1950.

[11] SCHMITZ-FEUERHAKE, I. Studies on three-dimensional scintigraphy with gamma - gamma – coincidences. **Phys. Med. Biol**, v. 15: p. 649–656, 1970.

[12] MONAHAN, W.G,; POWELL, M.D. Three-Dimensional Imaging of Radionuclide Distribution by Gamma-Gamma Coincidence Detection In: **Tomographic imaging in nuclear medicine**, p. 165–175, 1972.

[13] YAMAMOTO, S,; OKUMURA, S,; WATABE, T,; IKEDA, H,; KANAI, Y,; TOSHITO, T,; KOMORI, M,; OGATA, Y,; KATO, K,; HATAZAWA, J. Development of a prototype Open-close positron emission tomography system. **Rev. Sci. Instrum**, v. 86: p. 1–9, 2015.

[14] MASSARI, R,; D'ELIA, A,; SOLURI, A,; SOLURI, A. Super Spatial Resolution (SSR) method for small animal SPECT imaging: A Monte Carlo study. **Nucl. Instruments Methods Phys. Res. Sect. A Accel. Spectrometers, Detect. Assoc. Equip**, v. 982: 164584, 2020.

[15] SCOPINARO, F,; MASSARI, R,; VARVARIGOU AD, D'ALESSANDRIA, C,; TROTTA, C,; DI SANTO, G.P *et al.* High-resolution small animal single photon emission computed tomography: uptake of [99mTc] bombesin and [123I] ioflupane by rat brain. **Q J Nucl Med Mol Imaging**, v. 51, n. 2, p. 204-210, 2007.

[16] VAN AUDENHAEGE, K,; VAN HOLEN, R,; VANDENBERGHE, S,; VANHOVE, C,; METZLER, S.D,; MOORE, S.C. Review of SPECT collimator selection, optimization, and fabrication for clinical and preclinical imaging. **Med Phys**. 2015, v. 42(8): 4796-813. doi: 10.1118/1.4927061. PMID: 26233207; PMCID: PMC5148182.

[17] NKUBA, L.L,; OLSHANOSKI, K,; FUKUCHI, T,; LUGENDO, I.J,; DANG, N.P,; RANGACHARYULU, C,; SAI, K.V. Monte Carlo simulations of the non-collinear gamma-ray cascade emissions for medical imaging. *In*: 11th INTERNATIONAL CONFERENCE ON ISOTOPES (11-ICI) AND EXPO, Saskatoon, Canada, July 23-27, 2023.

[18] OLSHANOSKI, K,; NKUBA, L.L,; DANG, N.P,; FUKUCHI, T,; KANDA, H,; LUGENDO I.J, SAI, K.V,;RANGACHARYULU, C. Collimator design for gamma-ray cascade angular correlations in medical imaging. **J. Instrum**, v. 18 C05010, 2023.

[19] BUVAT, I,; CASTIGLIONI, I. Monte Carlo simulations in SPET and PET. **Q J Nucl Med**, v. 46, n. 1, p. 48-61, 2002.

[20] SANTIN, G,; STRUL, D,; LAZARO, D,; SIMON, L,; KRIEGUER, M,; VIEIRA, M.M, *et al.* GATE, a Geant4-based simulation platform for PET integrating movement and time management. **IEEE Nucl. Sci. Symp. Med. Imaging Conf**, v. 50, n. 5, p. 1516–1521, 2003.

[21] OKUMURA, S,; YAMAMOTO, S,; WATABE, H,; KATO, N,; HAMAMURA, H. Development of dual-layer GSO depth-of-interaction block detector using angled

optical fiber. **Nucl. Instruments Methods Phys. Res. Sect. A Accel. Spectrometers, Detect. Assoc. Equip,** v. 781, p. 65–70, 2015.

[22] FUKUCHI, T,; OKAUCHI, T,; SHIGETA, M,; YAMAMOTO, S,; WATANABE, Y,; ENOMOTO, S. Positron emission tomography with additional γ-ray detectors for multipletracer imaging. **Med. Phys***,* v. 44, p. 2257–2266, 2017.

[23] NKUBA, L.L,; LUGENDO, I.J,; AMOUR, I.S. A GATE-based Monte Carlo simulation of a dual-layer pixelized gadolinium oxyorthosilicate (GSO) detector performance and response for micro PET scanner. **Tanzania J. Sci***,* v. 47, n. 2, p. 507–519, 2021.

[24] BRUN, R,; RADEMAKERS, F. ROOT - An object oriented data analysis framework. **Nucl. Instruments Methods Phys. Res. Sect. A Accel. Spectrometers, Detect. Assoc. Equip**, v. 389, p. 81–86, 1997.

[25] GUNTER, D.L. Collimator characteristics and design. *In*: Henkin, R. E *et al.*(Ed), **Nuclear Medicine**. Mosby-Year Book, 96–124, St. Louis; 1996.

[26] GUNTER, D.L. Collimator Design for Nuclear Medicine. *In*: Wernick, M.N,; Aarsvold, J.N (Eds), **Emission Tomography. The Fundamentals of PET and SPECT**. Vol. X, 153–168, Elservia Academic Press. San Diego, Califonia; 2004.

[27] DEPREZ, K,; VANDENBERGHE, S,; VAN AUDENHAEGE, K,; VAN VAERENBERGH, J,; VAN HOLEN, R. Rapid additive manufacturing of MR compatible multipinhole collimators with selective laser melting of tungsten powder **Med. Phys**. 40: 1617–1634, 2013.

[28] SHIMAZOE, K,; UENOMACHI, M,; TAKAHASHI, H. 2022 Imaging and sensing of pH and chemical state with nuclear-spin-correlated cascade gamma rays via radioactive tracer. **Communications Physics 5,** Article No 24, p. 1-8, 2022.

[29] JIN, Y,; MENG, L.J. Exploration of Coincidence Detection of Cascade Photons to Enhance Preclinical Multi-Radionuclide SPECT Imaging. **IEEE Trans Med Imaging**. Doi: 10.1109/TMI.2023.3348756, 2024.

[30] UENOMACHI, M,; SHIMAZOE, K,; TAKAHASHI, H. A double photon coincidence detection method for medical gamma ray imaging. **Bio-Algorithms and Med-Systems**, v. 18, p. 120–126, 2022.

[31] SIMMS, P.C,; STEFFEN, R.M. Lifetime of the 247-keV excited state of ^{111}Cd. **Phys. Rev**. v. 108, p. 1459–1461, 1957.

[32] Open GATE Collaboration. Imaging Applications. Available at: https://opengate.readthedocs.io/en/latest/digitizer_and_detector_modeling.html#energy-resolution. Accessed on: 12 June 2024.

[33] MATULEWICZ, T,; KORZECKA, K,; PYTEL, Z. Tests of GSO scintillator In: **Annual Reports: Nuclear Physics Division**. (Eds S. Zygmunt & M. Popkiewicz), PL9800110, p. 48–49, 1996.

[34] ZHANG, C,; SANG, Z,; WANG, X,; ZHANG, X,; YANG, Y. The effects of inter-crystal scattering events on the performance of PET detectors. **Phys. Med. Biol**, v. 64, n. 20, p. 1-9, 2019.

[35] LIU, X,; LIU, H,; CHENG, L,; WU, J,; BAO, T,; YAO R,; LIU, Y. A 3-dimensional stationary cascade gamma ray coincidence imager. **Phys. Med. Biol***,* v. 66, n. 22: 225001, 2021.

[36] DU, J,; JONES, T. Technical opportunities and challenges in developing total-body PET scanners for mice and rats. **EJNMMI Physics***,* v. 10, n. 2, https://doi.org/10.1186/s40658-022-00523-6., 2023.

LICENSE